Monthly Notices
of the
ROYAL ASTRONOMICAL SOCIETY

Mon. Not. R. Astron. Soc. **410,** 1787–1796 (2011) doi:10.1111/j.1365-2966.2010.17559.x

Kepler observations of the beaming binary KPD 1946+4340

S. Bloemen,[1⋆] T. R. Marsh,[2] R. H. Østensen,[1] S. Charpinet,[3] G. Fontaine,[4] P. Degroote,[1] U. Heber,[5] S. D. Kawaler,[6] C. Aerts,[1,7] E. M. Green,[8] J. Telting,[9] P. Brassard,[4] B. T. Gänsicke,[2] G. Handler,[10] D. W. Kurtz,[11] R. Silvotti,[12] V. Van Grootel,[3] J. E. Lindberg,[8,13] T. Pursimo,[8] P. A. Wilson,[8,14] R. L. Gilliland,[15] H. Kjeldsen,[16] J. Christensen-Dalsgaard,[16] W. J. Borucki,[17] D. Koch,[17] J. M. Jenkins[18] and T. C. Klaus[19]

[1]*Instituut voor Sterrenkunde, Katholieke Universiteit Leuven, Celestijnenlaan 200D, B-3001 Leuven, Belgium*
[2]*Department of Physics, University of Warwick, Coventry CV4 7AL*
[3]*Laboratoire d'Astrophysique de Toulouse-Tarbes, Université de Toulouse, CNRS, 14 Av. E. Belin, 31400 Toulouse, France*
[4]*Département de Physique, Université de Montréal, C.P. 6128, Succ. Centre-Ville, Montréal, Québec H3C 3J7, Canada*
[5]*Dr. Remeis-Sternwarte & ECAP Astronomisches Institut, Univ. Erlangen-Nürnberg, Sternwartstr. 7, 96049 Bamberg, Germany*
[6]*Department of Physics & Astronomy, Iowa State University, Ames, IA 50011, USA*
[7]*Department of Astrophysics, IMAPP, Radboud University Nijmegen, PO Box 9010, NL-6500 GL Nijmegen, the Netherlands*
[8]*Steward Observatory, University of Arizona, 933 North Cherry Avenue, Tucson, AZ 85721, USA*
[9]*Nordic Optical Telescope, 38700 Santa Cruz de La Palma, Spain*
[10]*Institut für Astronomie, Universität Wien, Türkenschanzstrasse 17, 1180 Wien, Austria*
[11]*Jeremiah Horrocks Institute of Astrophysics, University of Central Lancashire, Preston, Lancashire PR1 2HE*
[12]*INAF-Osservatorio Astronomico di Torino, Strada dell'Osservatorio 20, 10025 Pino Torinese, Italy*
[13]*Centre for Star and Planet Formation, Natural History Museum of Denmark, University of Copenhagen, Øster Voldgade 5–7, DK-1350 Copenhagen, Denmark*
[14]*Institute of Theoretical Astrophysics, University of Oslo, PO Box 1029 Blindern, N-0315 Oslo, Norway*
[15]*Space Telescope Science Institute, 3700 San Martin Drive, Baltimore, MD 21218, USA*
[16]*Department of Physics and Astronomy, Aarhus University, DK-8000 Aarhus C, Denmark*
[17]*NASA Ames Research Center, MS 244-30, Moffett Field, CA 94035, USA*
[18]*SETI Institute/NASA Ames Research Center, MS 244-30, Moffett Field, CA 94035, USA*
[19]*Orbital Sciences Corp., NASA Ames Research Center, MS 244-30, Moffett Field, CA 94035, USA*

Accepted 2010 August 18. Received 2010 August 17; in original form 2010 June 5

ABSTRACT

The *Kepler Mission* has acquired 33.5 d of continuous 1-min photometry of KPD 1946+4340, a short-period binary system that consists of a subdwarf B star (sdB) and a white dwarf. In the light curve, eclipses are clearly seen, with the deepest occurring when the compact white dwarf crosses the disc of the sdB (0.4 per cent) and the more shallow ones (0.1 per cent) when the sdB eclipses the white dwarf. As expected, the sdB is deformed by the gravitational field of the white dwarf, which produces an ellipsoidal modulation of the light curve. Spectacularly, a very strong Doppler beaming (also known as Doppler boosting) effect is also clearly evident at the 0.1 per cent level. This originates from the sdB's orbital velocity, which we measure to be $164.0 \pm 1.9\,\mathrm{km\,s^{-1}}$ from supporting spectroscopy. We present light-curve models that account for all these effects, as well as gravitational lensing, which decreases the apparent radius of the white dwarf by about 6 per cent, when it eclipses the sdB. We derive system parameters and uncertainties from the light curve using Markov chain Monte Carlo simulations. Adopting a theoretical white dwarf mass–radius relation, the mass of the subdwarf is found to be $0.47 \pm 0.03\,\mathrm{M}_\odot$ and the mass of the white dwarf $0.59 \pm 0.02\,\mathrm{M}_\odot$. The effective temperature of the white dwarf is $15\,900 \pm 300$ K. With a spectroscopic effective temperature of $T_{\rm eff} = 34\,730 \pm 250$ K and a surface gravity of $\log g = 5.43 \pm 0.04$, the subdwarf has most likely exhausted its core helium, and is in a shell He burning stage.

⋆E-mail: steven.bloemen@ster.kuleuven.be

The detection of Doppler beaming in *Kepler* light curves potentially allows one to measure radial velocities without the need of spectroscopic data. For the first time, a photometrically observed Doppler beaming amplitude is compared to a spectroscopically established value. The sdB's radial velocity amplitude derived from the photometry ($168 \pm 4\,\mathrm{km\,s^{-1}}$) is in perfect agreement with the spectroscopic value. After subtracting our best model for the orbital effects, we searched the residuals for stellar oscillations but did not find any significant pulsation frequencies.

Key words: binaries: close – binaries: eclipsing – stars: individual: KPD 1946+4340 – subdwarfs.

1 INTRODUCTION

Subdwarf B stars (sdBs) are mostly assumed to be extreme horizontal branch stars, that is, core helium burning stars with a thin inert hydrogen envelope (Heber 1986; Saffer et al. 1994). In order to reach such high temperatures and surface gravities, the progenitor must have lost almost its entire hydrogen envelope. The majority of sdBs is expected to have lost its envelope via binary interaction channels, as elaborated by Han et al. (2002, 2003). Our target, KPD 1946+4340 (KIC 7975824), is an sdB with a white dwarf (WD) companion in a 0.403 739(8) d orbit (Morales-Rueda et al. 2003), which identifies the theoretical formation channel for this system as the second common-envelope ejection channel of Han et al. (2002, 2003). In this scenario, the WD is engulfed by the sdB progenitor as it ascends the first giant branch. The WD will deposit its angular momentum in the atmosphere of the giant and spin up the envelope until it is ejected. There are two subchannels to this scenario, depending on the initial mass of the progenitor. If sufficiently massive, it will ignite helium non-degeneratively, and the resulting extended horizontal branch (EHB) star will have a mass of $\sim$0.35 $\mathrm{M}_\odot$. The more common scenario, starting with a roughly solar-mass giant, produces an EHB star with a mass that must be very close to the helium flash mass of 0.47 $\mathrm{M}_\odot$. A third possibility occurs when the WD companion ejects the envelope before the core has attained sufficient mass to ignite helium. In this case, the remaining core will evolve directly to the WD cooling track. On its way it crosses the domain of the EHB stars, but without helium ignition the period for which it appears as an sdB star is brief, making this channel a very small contributor to the sdB population. For a recent extensive review on hot subdwarf stars, their evolution and observed properties, see Heber (2009).

The exact physical details involved in common-envelope ejection are not well understood. This uncertainty is commonly embodied in the efficiency parameter α, which denotes the amount of orbital energy used to eject the envelope (see e.g. de Kool 1990; Hu et al. 2007). Eclipsing subdwarf binaries could help constrain the permitted values of α, but studies have hitherto been hampered by the fact that both sdB+WD and sdB+M-dwarf binaries have virtually invisible companions and are therefore single lined, leaving the masses indeterminate. Firmly establishing the parameters of both components of a post-CE system therefore has substantial implications not just for confirming that our formation scenarios are correct, but also in order to tune future binary population synthesis studies by confining the α parameter.

The target studied here, KPD 1946+4340, is an sdB star discovered by the Kitt Peak Downes survey (Downes 1986). KPD 1946+4340 has a V-band magnitude of 14.284 ± 0.027 (Allard et al. 1994), a y magnitude of 14.299 ± 0.002 (Wesemael et al. 1992) and a *Kp* (*Kepler*) magnitude of 14.655. The star was included in the radial velocity survey of Morales-Rueda et al. (2003), who found the target to be a spectroscopic binary with a period of 0.403 739(8) d and a velocity amplitude $K_1 = 167 \pm 2\,\mathrm{km\,s^{-1}}$. They also concluded that the sdB primary should be in a post-EHB stage of evolution, due to its relatively low surface gravity, placing it above the canonical EHB in the Hertzsprung–Russell diagram. This implies that the sdB exhausted all available helium in its core and is now in a shell helium burning stage. Assuming the sdB mass to be 0.5 $\mathrm{M}_\odot$, they found a minimum mass of 0.628 $\mathrm{M}_\odot$ for the companion.

In this paper we present the first light curve of KPD 1946+4340 obtained from space. The target was observed for 33.5 d by the *Kepler Mission*, and the light curve reveals sufficient low-level features to permit purely photometric measurements of velocities, radii and masses of both components. A review of the *Kepler Mission* and its first results is given in Koch et al. (2010).

We combine the *Kepler* photometry with new and old spectroscopic measurements, use light-curve modelling to estimate the system parameters and Markov chain Monte Carlo (MCMC) simulations to establish the uncertainties. The relativistic Doppler beaming effect is clearly detected in the light curve, and can be used to determine the orbital velocity of the primary. This effect, which is also known as Doppler boosting, was recently noted in a *Kepler* light curve of KOI-74 by van Kerkwijk et al. (2010). We present the first comparison of a radial velocity amplitude as derived from the amplitude of the Doppler beaming to the spectroscopically determined value. We also use the spectroscopic data to provide a revised ephemeris, as well as to determine the effective temperature, surface gravity and helium fraction of the atmosphere. After detrending the *Kepler* light curve with our best model for the orbital effects, we search the residuals for stellar oscillations.

2 OBSERVATIONS, RADIAL VELOCITIES AND UPDATED EPHEMERIS

We used 33.5 d of Q1 short cadence *Kepler* data with a time resolution of 59 s. A review of the characteristics of the first short cadence data sets is presented by Gilliland et al. (2010b). The data were delivered to us through the *Kepler* Asteroseismic Science Operations Center (KASOC) website.[1] The level of contamination of the fluxes by other stars is poorly known. We used the raw fluxes and assumed

[1] http://kasoc.phys.au.dk/kasoc/

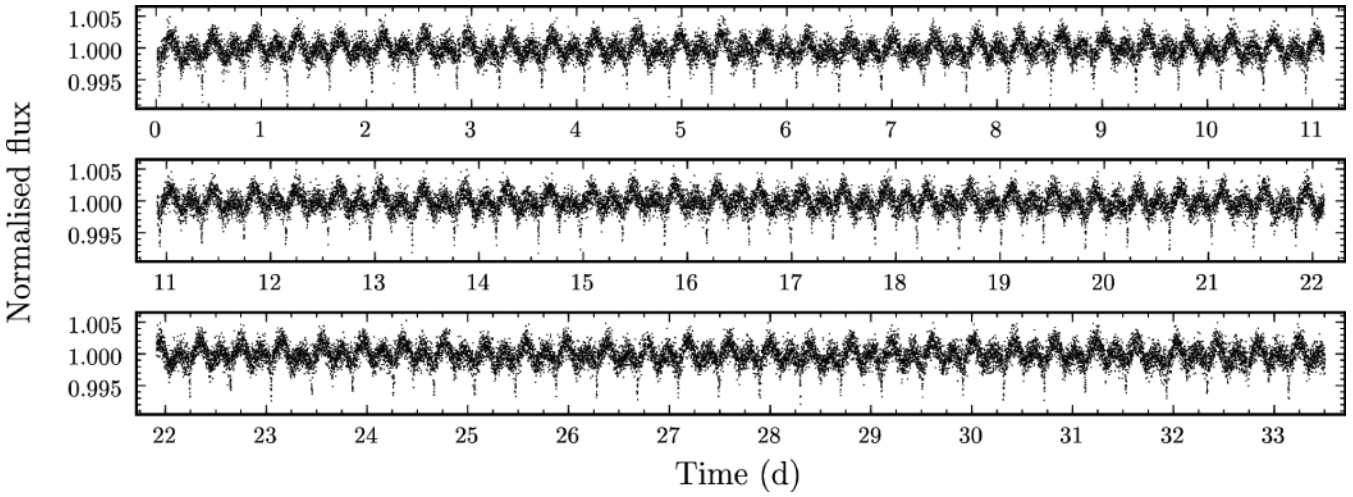

Figure 1. *Kepler* light curve of KPD 1946+4340 after detrending and removing outliers.

zero contamination, which is justified by the absence of other significantly bright sources within 10 arcsec of KPD 1946+4340. We applied a barycentric correction to the *Kepler* timings and converted them from UTC to barycentric dynamical time (TDB). The raw data show a ∼2 per cent downward trend over the 33.5 d, which we assume is instrumental in origin. We removed this variation by fitting and dividing out a spline function. Out of the original data set of 49170, we rejected 54 points because of a bad quality flag. After initial light-curve model fits to be described below, we then rejected another 87 points, because they differed by more than 3.5σ from our model. The full light curve we used for our analysis is shown on Fig. 1. The time-span of the data set is BMJD(TDB)[2] 54 964.003 14 to 54 997.493 81.

The high signal-to-noise ratio (S/N) spectra from Green et al. (2008) were used to derive $T_{\rm eff}$ and $\log g$; see Section 4 for details.

To refine the orbital period determination of Morales-Rueda et al. (2003), spectra were collected with the 2.56-m Nordic Optical Telescope (NOT) on 2009 December 5, 9 and 10. Using the ALFOSC spectrograph and a 0.5-arcsec slit, we obtained eleven spectra with exposure times of 300 s and a of resolution $R \sim 2000$, covering a wavelength region of 3500–5060 Å. We measured the radial velocities using multi-Gaussian fits (Morales-Rueda et al. 2003); the values are listed in Table 1. We first fitted the data of Morales-Rueda et al. (2003) and the new data separately to determine their rms scatter. From these fits we found that it was necessary to add 3.6 and 4.1 km s^{-1} in quadrature to the uncertainties of the two data sets to deliver a unit χ^2 per degree of freedom; these values probably reflect systematic errors due to incomplete filling of the slit. We then carried out a least-squares sinusoidal fit to the combined data set finding a best fit of $\chi^2 = 21.6$ (25 points). The next best alias had $\chi^2 = 39$, and so we consider our best alias to be the correct one. This gave the following spectroscopic ephemeris:

$$\mathrm{BMJD(TDB)} = 53\,652.848\,13(62) + 0.403\,750\,26(16)E,$$

marking the times when the sdB is closest to the Earth. The corresponding radial velocity amplitude was $K_1 = 164.0 \pm 1.9$ km s^{-1}. The WD's spectrum will slightly reduce the observed velocity amplitude of the sdB. We estimate that this effect is less than 1 km s^{-1}. The radial velocity measurements and the fit are shown in Fig. 2.

[2] BMJD(TDB) refers to Barycentric-corrected Modified Julian Date on the Barycentric Dynamical Time-scale.

Table 1. Radial velocities (RVs) of the sdB in KPD 1946+4340 determined from NOT spectroscopy.

BMJD(TDB)	RV (km s^{-1})
55 170.811 18	−139.8 ± 3.5
55 170.862 68	−162.0 ± 3.3
55 170.907 43	−109.2 ± 3.8
55 170.958 96	22.5 ± 5.7
55 174.809 52	−73.5 ± 3.0
55 174.849 99	−154.7 ± 3.3
55 174.902 91	−171.9 ± 4.0
55 174.932 20	−127.6 ± 4.7
55 175.800 06	2.3 ± 4.4
55 175.843 79	102.4 ± 4.7
55 175.883 28	148.3 ± 6.5

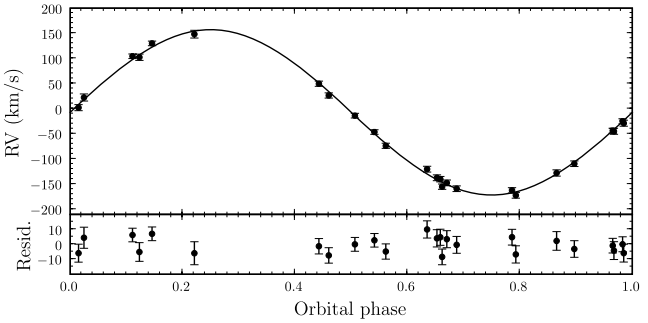

Figure 2. Radial velocity curve of the sdB in KPD 1946+4340. Both our new radial velocity measurements and the ones from Morales-Rueda et al. (2003) are shown, folded on the orbital period. The error bars of the data points show the uncertainties after adding 3.6 and 4.1 km s^{-1} in quadrature to the values of Morales-Rueda et al. (2003) and our new data, respectively. We find a radial velocity amplitude of $K_1 = 164.0 \pm 1.9$ km s^{-1}.

From fitting light-curve models to the *Kepler* photometry (see Section 3.3), we derived the following photometric ephemeris:

$$\mathrm{BMJD(TDB)} = 54\,979.975\,296(25) + 0.403\,750\,00(96)E.$$

The two independent periods agree to within their uncertainties. The 9-yr baseline of the spectroscopic ephemeris gives a

more precise value and henceforth we fix it at this value in our lightcurve models. The cycle count between the spectroscopic and photometric ephemerides (using the spectroscopic period) is 3287.0001 ± 0.0015, an integer to within the uncertainties. The *Kepler*-based zero-point is the more precise one and is therefore retained as a free parameter in our models.

3 LIGHT-CURVE ANALYSIS

The *Kepler* light curve we analyse in this paper (Fig. 1) reveals that KPD 1946+4340 is an eclipsing binary. We graphically determined the eclipse depths and durations. The eclipses of the WD by the sdB are 0.13 ± 0.03 per cent deep and the eclipses of the sdB by the WD are 0.38 ± 0.03 per cent. The duration of the eclipses at half maximum depth is 0.0236 ± 0.0003 in orbital phase units. There is a clear asymmetric ellipsoidal modulation pattern in which the flux maximum after the deeper eclipses is larger than the maximum after the shallower eclipses. We attribute this to Doppler beaming, see Section 3.2.

To determine the system properties, we modelled the light curve with the LCURVE code written by TRM (for a description of the code, see Copperwheat et al. 2010, appendix A). This code uses grids of points to model the two stars, taking into account limb darkening, gravity darkening, Doppler beaming and gravitational lensing when the WD eclipses its companion. It assumes the ellipsoidally deformed star to be in corotation with the binary orbit, which is usually a good assumption because of the large tidal interactions between the two binary components. Reprocessing of light from the sdB by the WD is included in the light-curve models as well ('reflection effect').

To speed up the computation of the models used in this paper we implemented a new option whereby a finer grid can be used along the track of the WD as it eclipses the sdB. This reduces the overall number of points needed to model the light curve to the demanding precision required to model the *Kepler* data. In addition, we only used the finely-spaced grid during the eclipse phases, taking care to make the model values continuous when changing between grids by applying normalisation factors (very close to unity) to the coarse grid fluxes. We used $\sim$100 000 ($\sim$37 000) grid points for the fine (coarse) grids for the sdB and 3000 for the WD. To model the finite exposures more accurately during the eclipses, where smearing occurs due to the 1 m integration time, we calculated seven points for each exposure (i.e. one point for every $\sim$10 s) and took their trapezoidal average.

3.1 Gravity darkening and limb darkening coefficients

We used model spectra to compute the gravity darkening coefficient (GDC) of the sdB and the limb darkening coefficients for both the sdB and the WD, which are all important parameters for the modelling of a close binary's light curve. The GDC is needed to model the effects of the WD's gravity on the sdB, which slightly distorts the sdB's shape. The bolometric flux from a stellar surface depends on the local gravity as $T^4 \propto g^{\beta_\mathrm{b}}$, where β_b is the bolometric GDC. For radiative stars, $\beta_\mathrm{b} = 1$ (von Zeipel 1924). We observe the band-limited stellar flux, not the bolometric flux, and hence we require a different coefficient defined by $I \propto g^{\beta_\mathrm{K}}$. The GDC for the *Kepler* bandpass, β_K, was computed from

$$\beta_\mathrm{K} = \frac{\mathrm{d}\log I}{\mathrm{d}\log g} = \frac{\partial \log I}{\partial \log g} + \frac{\partial \log I}{\partial \log T}\frac{\mathrm{d}\log T}{\mathrm{d}\log g}, \quad (1)$$

where I is the photon-weighted bandpass-integrated specific intensity at $\mu = 1$ and $\frac{\mathrm{d}\log T}{\mathrm{d}\log g} = \frac{\beta_\mathrm{b}}{4} = 0.25$. We used a grid of sdB atmosphere models calculated from the local thermodynamic equilibrium (LTE) model atmosphere grid of Heber, Reid & Werner (2000) using the Linfor program (Lemke 1997) and assumed $T_\mathrm{eff} = 34\,500$ K, $\log g = 5.5$, $\log(n_\mathrm{He}/n_\mathrm{H}) = -1.5$ and $\log(Z/Z_\odot) = -2$. To estimate the interstellar reddening, we compared the observed $B - V$ colour of -0.20 ± 0.01 mag (Allard et al. 1994) with the colours expected from a model atmosphere. We found an intrinsic colour of $B - V = -0.26$ mag and consequently adopted a reddening of $E(B - V) = 0.06$. To account for this interstellar reddening the model spectra were reddened following Cardelli, Clayton & Mathis (1989). The GDC was found to be $\beta_\mathrm{K} = 0.448$.

Using a model for the same set of parameters, we computed limb darkening coefficients for the sdB. We adopted the four-parameter limb darkening relation of Claret (2004, equation 5) and determined $a_1 = 0.818$, $a_2 = -0.908$, $a_3 = 0.755$ and $a_4 = -0.252$.

For the WD, angle-dependent model spectra were calculated using the code of Gänsicke, Beuermann & de Martino (1995) for $T_\mathrm{eff} = 17\,000$ K (estimated from a comparison of model surface brightnesses given initial light-curve fits) and $\log g = 7.8$. We adopted the same limb darkening law as for the sdB and found $a_1 = 0.832$, $a_2 = -0.681$, $a_3 = 0.621$ and $a_4 = -0.239$.

3.2 Doppler beaming factor

The asymmetry in KPD 1946+4340's ellipsoidal modulation pattern is the result of Doppler beaming. Doppler beaming is caused by the stars' radial velocity shifting the spectrum, modulating the photon emission rate and beaming the photons somewhat in the direction of motion. The effect was, as far as we are aware, first discussed in Hills & Dale (1974) for rotation of WDs and by Shakura & Postnov (1987) for orbital motion in binaries. It was first observed by Maxted, Marsh & North (2000). Its expected detection in *Kepler* light curves was suggested and discussed by Loeb & Gaudi (2003) and Zucker, Mazeh & Alexander (2007). van Kerkwijk et al. (2010) report the detection of Doppler beaming in the long cadence *Kepler* light curve of the binary KOI-74. For the first time, they measured the radial velocity of a binary component from the photometrically detected beaming effect. The measured radial velocity amplitude, however, did not match the amplitude as expected from the mass ratio derived from the ellipsoidal modulation in the light curve. The derived velocity of the primary of KOI-74 is yet to be confirmed spectroscopically. For KPD 1946+4340, radial velocities are available which allows the first spectroscopic check of a photometrically determined radial velocity.

For radial velocities that are much smaller than the speed of light, the observed flux F_λ is related to the emitted flux $F_{0,\lambda}$ as

$$F_\lambda = F_{0,\lambda}\left(1 - B\frac{v_r}{c}\right), \quad (2)$$

with the beaming factor $B = 5 + \mathrm{d}\ln F_\lambda/\mathrm{d}\ln\lambda$ (Loeb & Gaudi 2003). The beaming factor thus depends on the spectrum of the star and the wavelength of the observations. For the broadband *Kepler* photometry, we use a photon weighted bandpass-integrated beaming factor

$$\langle B\rangle = \frac{\int \epsilon_\lambda \lambda F_\lambda B\,\mathrm{d}\lambda}{\int \epsilon_\lambda \lambda F_\lambda\,\mathrm{d}\lambda} \quad (3)$$

in which ϵ_λ is the response function of the *Kepler* bandpass.

We determined the beaming factor from a series of fully metal line-blanketed LTE models (Heber et al. 2000, see also Section 3.1)

with metallicities ranging from $\log(Z/Z_\odot) = -2$ to $+1$, as well as from non-LTE models with zero metals and with Blanchette metal composition (see Section 4 of this paper for more information about the non-LTE models). Without taking reddening into account, the beaming factor is found to be $\langle B \rangle = 1.30 \pm 0.03$. The uncertainty incorporates the dependence of the beaming factor on the model grids and the uncertainty on the sdB's effective temperature, gravity and, most importantly, metallicity. The metal composition of the model atmospheres is a poorly known factor that can only be constrained with high-resolution spectroscopy.

This time, the effect of reddening has to be accounted for by changing the spectral response accordingly instead of reddening the model atmosphere spectrum. Using a reddened spectrum would in this case erroneously imply that the reddening is caused by material that is comoving with the sdB star. With reddening, the beaming factor is determined to be ∼0.006 lower. Reddening thus only marginally affects the beaming of KPD 1946+4340 but should certainly be taken into account in case of higher reddening values.

There are three contributions to the beaming factor. The enhanced photon arrival rate of an approaching source contributes $+1$ to the beaming factor. Aberration also increases the number of photons that is observed from an approaching source, adding $+2$ to the beaming factor because of the squared relation between the normal angle and solid angle. Finally, when the sdB comes towards us, an observed wavelength, λ_o, corresponds to an emitted wavelength $\lambda_e = \lambda_o\,(1 + v_r/c)$. Since sdBs are blue, looking at a longer wavelength reduces the observed flux which counteracts the other beaming factor components. In case of an infinite temperature Rayleigh–Jeans spectrum, this Doppler shift contribution to the beaming factor would be -2. For the primary of KPD 1946+4340, we find a contribution of ~ -1.70 which brings the total beaming factor to ∼1.30. The contribution of the Doppler shift does not always have to be negative; a red spectrum could actually increase the effect of beaming.

3.3 Light-curve model

A typical fit to the data is shown in Fig. 3, with the different contributions switched on, one-by-one. From the residuals (bottom panel), it is clear that the model reproduces the variations at the orbital period very well. When we fit the light curve outside the eclipses with sine curves to represent the reflection effect, ellipsoidal modulation and the beaming, the phase of the ellipsoidal modulation is found to be off by 0.0072 ± 0.0010 in orbital phase units. We do not know the origin of this offset, which also gives rise to the shallow structure that is left in the residuals. Our best fits have $\chi^2 = 52\,032$ for 48 929 data points.

The significance of the Doppler beaming is obvious, and even the more subtle gravitational lensing effect is very significant, although it cannot be independently deduced from the data since it is highly degenerate with changes in the WD's radius and temperature. One part of the gravitational lensing is caused by light from the sdB that is bent around the WD, effectively making the WD appear smaller. The second lensing contribution is a magnification effect, which is caused by the altered area of the sdB that is visible, given that surface brightness is conserved by the lensing effect. In the case of KPD 1946+4340, the first part of the lensing is the most important. Lensing effects in compact binaries were discussed in, for example, Maeder (1973), Gould (1995), Marsh (2001) and Agol (2002, 2003). Sahu & Gilliland (2003) explored the expected influence of microlensing effects on light curves of compact binaries and planetary systems observed by *Kepler*. They found that the lensing effect

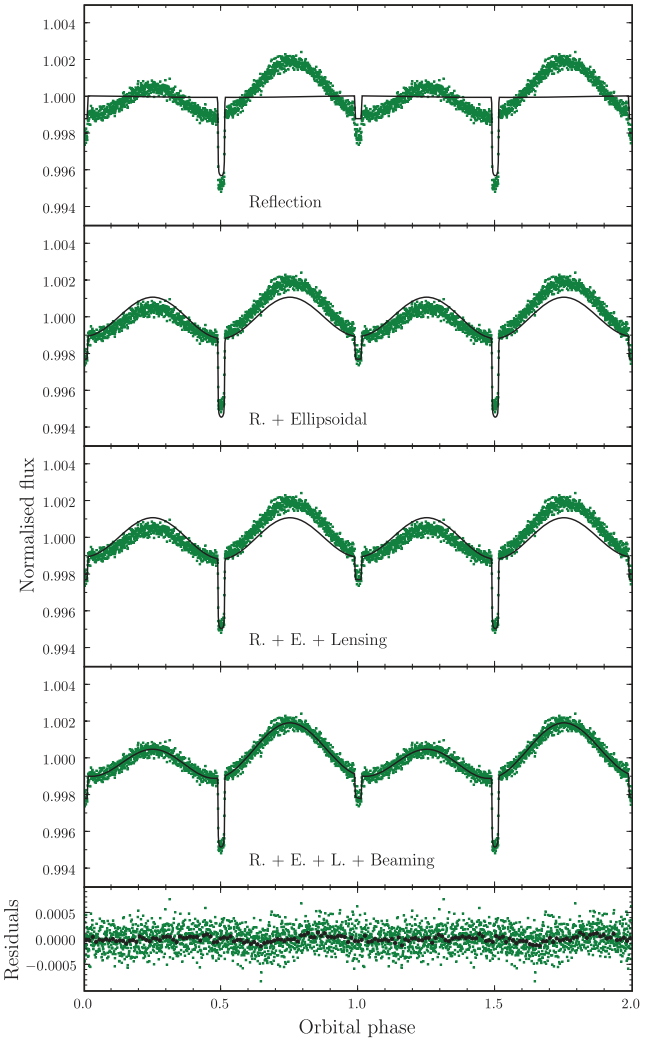

Figure 3. Phase-folded light curve of KPD 1946+4340 (green, data points grouped by 30) and our best-fitting model (black). In the top panel, only the eclipses and reflection effects are modelled. In the second panel, ellipsoidal modulation is added. In the third panel, gravitational lensing is taken into account as well, which affects the depth of the eclipse at orbital phase 0.5. The bottom panels show the full model – taking into account Doppler beaming – and the residuals (grouped by 30 in green and grouped by 600 in black).

of a typical WD at 1 au of a main-sequence star will swamp the eclipse signal. A transit of a planet, which is of similar size but a lot less massive, can therefore easily be distinguished from an eclipse by a WD. In the case of KPD 1946+4340, the separation of the two components is a lot less. An eclipse is still seen, but with reduced depth. For the most likely system parameters, gravitational lensing reduces the eclipse depth by ∼12 per cent which is equivalent to a ∼6 per cent reduction of the apparent WD radius. The effect of gravitational lensing is implemented in our light-curve modelling code following Marsh (2001).

3.4 Markov chain Monte Carlo simulation

The parameters which determine models can be fixed by minimization of χ^2. If the S/N is high, a quadratic approximation around the point of minimum χ^2 can lead to the uncertainties of, and correlations between, the best-fit parameters. The *Kepler* data have a

superb S/N, but owing to the very shallow depths of the eclipses, the quadratic approximation does not work well. Strong correlations between several parameters play a significant role in this problem. The duration of the eclipses essentially fixes the scaled radius of the sdB star (which we take to be the primary) $r_1 = R_1/a$, where a is the binary separation. The scaled radius is a function of orbital inclination i, $r_1 = r_1(i)$. The depth of the eclipse of the sdB by the WD fixes the ratio of radii $r_2/r_1 = R_2/R_1$, so r_2 is also a function of orbital inclination. The duration of the ingress and egress features provides an independent constraint on r_2 as a function of i, which can break the degeneracy. In this case, however, one is limited by a combination of the S/N and minute-long cadence, which is not sufficient to resolve the ingress/egress features.

Under these circumstances, an MCMC method can be very valuable. The MCMC method allows one to build up a sequence of models in which the fitting parameters, which we denote by the vector $\boldsymbol{a}$, have a probability distribution matching the Bayesian posterior probability of the parameters given the data, $P(\boldsymbol{a}|\boldsymbol{d})$. From long chains of models one can then calculate variances and plot confidence regions. The MCMC method also has the side benefit of helping with the minimization, which can become difficult when parameters are highly correlated. For data in the form of independent Gaussian random variables, this probability can be written as

$$P(\boldsymbol{a}|\boldsymbol{d}) \propto P(\boldsymbol{a})\mathrm{e}^{-\chi^2/2}, \quad (4)$$

that is, the product of one's prior knowledge of the model parameters and a factor depending upon the goodness of fit as expressed in χ^2. We implemented the MCMC method following procedures along the line of Collier Cameron et al. (2007). We incorporated prior information in two ways. In all cases we used our constraint $K_1 = 164 \pm 2\,\mathrm{km\,s^{-1}}$. Using our own spectroscopic analysis and the results of Morales-Rueda et al. (2003), we decided to put also the following constraint on the effective temperature of the sdB: $T_1 = 34\,500 \pm 400$ K. These two constraints were applied by computing the following modified version of χ^2:

$$-2\ln(P(\boldsymbol{a}|\boldsymbol{d})) = \chi^2 + \left(\frac{K_1 - 164}{2}\right)^2 + \left(\frac{T_1 - 34\,500}{400}\right)^2, \quad (5)$$

where K_1 and T_1 are the values in the current MCMC model under test. The period of the binary orbit was kept fixed at the spectroscopically determined value (see Section 2). The parameters that were kept free during the modelling are the scaled stellar radii R_1/a and R_2/a, the mass ratio q, the inclination i, the effective temperature of the WD T_2, the beaming factor and the zero-point of the ephemeris. The radial velocity scale (which leads to the masses M_1 and M_2) and the effective temperature of the primary T_1 were included in the fits as well, but with the spectroscopically allowed range as a prior constraint. Note that the beaming factor $\langle B \rangle$ is kept as a free parameter, which allows the code to fit the Doppler beaming amplitude while we constrain the allowed range of K_1. By comparing the MCMC results for $\langle B \rangle$ with the theoretical beaming factor, we can check if the beaming amplitude is consistent with our expectations.

As explained above, this led to parameter distributions with strong correlations between R_1, R_2, M_1, M_2, q, etc. The mass–radius relations for the two stars are shown in Fig. 4. The favoured parameters for the secondary (left panel) clearly show that it is a WD and the allowed distribution nicely crosses the expected track of mass–radius (solid green line), which we calculated from the zero temperature relation of Eggleton (quoted in Verbunt & Rappaport 1988), inflated by a factor of 1.08. We estimated this factor from the cooling models of Holberg & Bergeron (2006) for WDs with a mass between 0.5 and 0.7 $\mathrm{M}_\odot$ (WDs with masses outside this range are ruled out by the mass–radius relation) using our preferred temperature for the WD of around 16 000 K and assuming an envelope that consists of $M_\mathrm{H} = 10^{-4}\,M_\mathrm{WD}$ and $M_\mathrm{He} = 10^{-2}\,M_\mathrm{WD}$.

Given that the secondary is a WD and given that the secondary's theoretical mass–radius relation intersects the mass–radius distribution very nearly within the 1σ region, we also undertook MCMC runs where we added the prior constraint that the secondary had to match the WD mass–radius relation to within an rms of 5 per cent. This was added in exactly the same manner as the K_1 and T_1 constraints. The system parameters we derive from these MCMC runs are listed in Table 2. The mass–radius relation after applying the constraint is shown in Fig. 5. Especially after applying the WD mass–radius relation constraint, the sdB's mass–radius relation fits

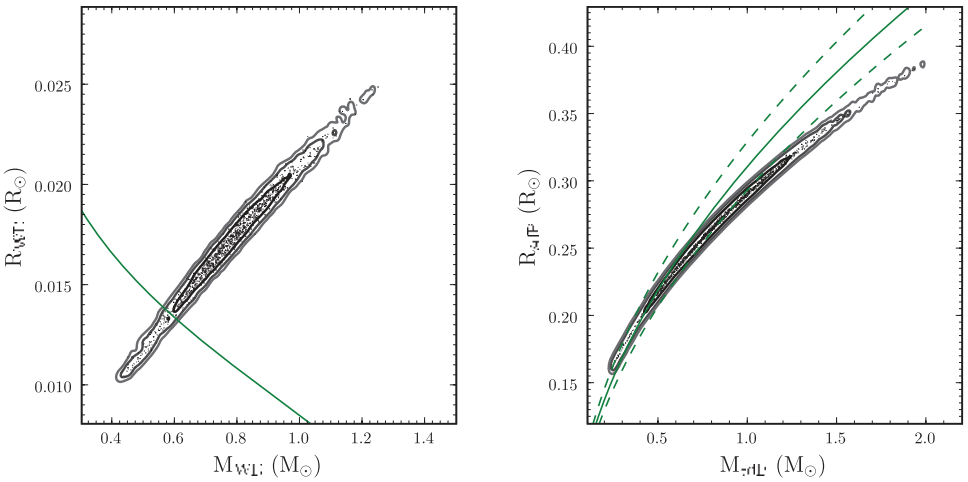

Figure 4. Mass–radius relations of the WD (left-hand panel) and sdB (right-hand panel). One-tenth of our MCMC models are shown (black dots). The contour plots show the regions in which 68, 95 and 99 per cent of the models reside. The contours that are shown are somewhat artificially broadened by the binning process. The Eggleton mass–radius relation, inflated by a factor of 1.08 to allow for the finite WD temperature (see text for details), is shown as a solid green track on the left-hand plot. The mass–radius relation intersects the Eggleton relation very nearly within its 1σ region. On the right-hand panel, the solid green line gives the mass–radius relation for $\log g = 5.45$, the dashed lines give the mass–radius relation for $\log g = 5.40$ (left-hand side) and $\log g = 5.50$ (right-hand side).

Table 2. Properties of KPD 1946+4340. The orbital period and the effective temperature of the sdB were derived from spectroscopy. The other parameters are obtained by modelling the *Kepler* light curve. The uncertainties on these values are determined by an MCMC analysis, using the prior constraint that the WD mass–radius relation has to match the Eggleton relation to within 5 per cent rms.

	Primary (sdB)	Secondary (WD)
$P_{\rm orb}$ (d)	0.403 750 26(16)	
q	1.27 ± 0.06	
i (°)	87.14 ± 0.15	
R ($R_\odot$)	0.212 ± 0.006	0.0137 ± 0.0004
M ($M_\odot$)	0.47 ± 0.03	0.59 ± 0.02
$T_{\rm eff}$ (K)	$34\,500 \pm 400$	$15\,900 \pm 300$

perfectly with the one defined by the surface gravity derived from spectroscopy in Section 4. The correlation coefficients between the different parameters are given in Table 3. The binary's inclination, its mass ratio and the stellar radii are highly correlated.

3.5 Variability in residuals

One of the goals of the *Kepler Mission* is to allow detailed asteroseismic studies of pulsating stars. The asteroseismology programme is discussed in Gilliland et al. (2010a). For more information about the search for pulsations in compact objects with *Kepler*, see Østensen et al. (2010a).

The Fourier transform of the original light curve of an eclipsing close binary like KPD 1946+4340 is highly contaminated by frequencies and their harmonics due to the binary orbit. Subtraction of a good model of the binary signatures of the light curve allows one to get rid of this contamination. Since a number of sdBs have been found to be multiperiodically pulsating (for a review on asteroseismology of EHB stars, see Østensen 2009), we checked the residuals of the light curve for signs of pulsations. Using the analysis method and significance criteria outlined in Degroote et al. (2009), eight significant frequencies were found, which are listed in Table 4.

f_2 is a known artefact frequency caused by an eclipsing binary that was used as one of the fine-guidance stars during Q1 (see Haas et al. 2010; Jenkins et al. 2010). Four other frequencies (f_1, f_3, f_4 and f_5) are related to f_2. The highest frequency, f_6, is related to the processing of the long cadence data (see Gilliland et al. 2010b). f_7 is the first harmonic of the orbital frequency of KPD 1946+4340, which indicates that there is still a weak orbital component left after subtracting our light-curve model. f_8 is not related to any of the other frequencies and corresponds to a period that is too long to arise from stellar pulsations of the WD or the sdB. If it is real, the signal might result from the rotation of the WD, or it might be due to a background star.

The best candidate peak for p-mode pulsations of the sdB is at 5018.2 μHz with an amplitude of 37 μmag, but further data are needed to confirm that the sdB is pulsating. From ground-based

Table 3. Correlation coefficients of the different parameters that were varied in the MCMC simulations, after applying the Eggleton mass–radius relation constraint.

	R_2	i	T_1	T_2	q
R_1	0.95	−0.95	0.02	0.02	−0.95
R_2		−0.98	0.07	0.02	−0.99
i			−0.06	−0.02	0.96
T_1				0.44	−0.09
T_2					−0.02

Table 4. Significant variability frequencies in the residuals of the light curve of KPD 1946+4340. The value of the S/N was determined by dividing the amplitude of the peak with the uncertainty on the amplitude.

	Frequency (d^{-1})	Amplitude (μmag)	S/N	
f_1	0.2758 ± 0.0011	97.5 ± 7.2	13.5	$=f_2/2$
f_2	0.5936 ± 0.0013	97.5 ± 7.2	13.5	Instrumental
f_3	0.1417 ± 0.0014	86.6 ± 7.2	12.1	$=f_2/4$
f_4	1.1820 ± 0.0015	81.0 ± 7.2	11.3	$=2f_2$
f_5	1.7730 ± 0.0018	67.5 ± 7.2	9.4	$=3f_2$
f_6	440.4386 ± 0.0022	54.2 ± 7.2	7.6	Instrumental
f_7	4.9548 ± 0.0024	49.1 ± 7.2	6.9	$=2f_{\rm orb}$
f_8	0.3115 ± 0.0027	44.9 ± 7.2	6.3	

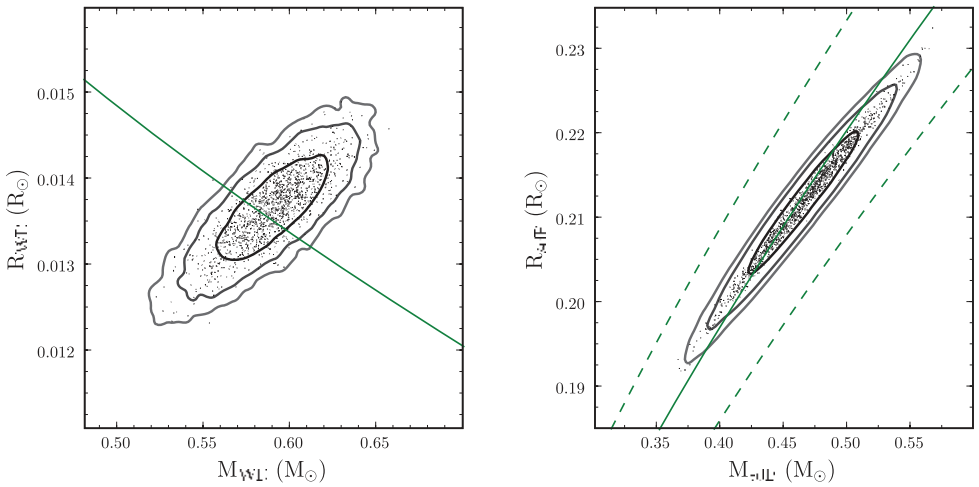

Figure 5. Figure equivalent to Fig. 4, but for an MCMC run with a prior constraint that the WD mass–radius relation has to match the Eggleton relation to within 5 per cent rms.

data, Østensen et al. (2010b) did not detect pulsations, with a limit of 0.68 mma. This is consistent with the *Kepler* photometry.

4 SPECTROSCOPIC ANALYSIS

Low-resolution high-S/N spectra for KPD 1946+4340 were taken with the B&C spectrograph at Steward Observatory's 2.3-m Bok telescope on Kitt Peak, as part of a long-term homogeneous survey of hot subdwarf stars (Green et al. 2008), in 2004 September and October. The spectrograph parameters, observational procedures and reduction techniques were kept the same for all the observing nights.

The 400/mm grating, blazed at 4889 Å, gives a resolution of $R = 560$ over the wavelength region 3620–6895 Å, when used with the 2.5-arcsec slit. The spectra were taken during clear or mostly clear conditions with integration times between 1050 and 1200 s. Approximately 1000 bias and flat-field images were obtained for each run. The data reductions were performed using standard IRAF tasks, and each night was flux-calibrated separately. The individual spectra were cross-correlated against a super-template to determine the relative velocity shifts, and then shifted and combined into a single spectrum. Although the resolution is rather low, the S/N is quite high: 221/pixel or 795/resolution element for the combined spectrum. The continuum fit to the combined flux-calibrated spectrum was done with great care to select regions devoid of any weak lines, including expected unresolved lines of heavier elements.

The final KPD 1946+4340 spectrum was fitted using two separate grids of non-LTE models designed for sdB stars, in order to derive the effective temperature, surface gravity and He/H ratio. The first set of models assumed zero metals, while the second included an adopted distribution of metals based on the analysis of FUSE spectra of five sdB stars by Blanchette et al. (2008), see also Van Grootel et al. (2010). From the set of models without metals, we derive $\log g = 5.45 \pm 0.04$, $T_{\rm eff} = 34\,400 \pm 220$ K and $\log({\rm He/H}) = -1.37 \pm 0.05$. Assuming the Blanchette composition, we find $\log g = 5.43 \pm 0.04$, $T_{\rm eff} = 34\,730 \pm 250$ K and $\log({\rm He/H}) = -1.36 \pm 0.04$. These results are in good agreement with $\log g = 5.37 \pm 0.10$, $T_{\rm eff} = 34\,500 \pm 1000$ K, $\log({\rm He/H}) = -1.35 \pm 0.10$ determined by Morales-Rueda et al. (2003) and $\log g = 5.43 \pm 0.10$, $T_{\rm eff} = 34\,200 \pm 500$ K determined by Geier et al. (2010) using different spectra and model grids.

The fit definitely improves when going from the zero-metal solution (Fig. 6) to the Blanchette composition (Fig. 7), although there still remains a slight 'Balmer' problem, especially noticeable in the core of Hβ. There are definitely metals in the spectrum of KPD 1946+4340: the strongest features are (1) an unresolved C III + N II complex around 4649 Å (compare the two figures for that feature) and (2) another weaker complex (C III + O II) in the blue wing of Hδ that the Blanchette model reproduces quite well. All of the major discrepancies between the spectra and the models are due to strong interstellar absorption: the K line of Ca II in the blue wing of Hϵ, the Ca II H line in the core of Hϵ and the Na I doublet strongly affecting the red wing of He I 5876. It is reassuring that the derived atmospheric parameters are not too strongly dependent on the presence of metals, as might be expected for such a hot star, particularly one in which downward diffusion of metals is important.

5 DISCUSSION

The beaming factor we derived for KPD 1946+4340 using MCMC runs is $\langle B \rangle = 1.33 \pm 0.02$, which is in perfect agreement with the theoretically expected value calculated in Section 3.2. The uncertainty on the beaming factor is a direct reflection of the uncertainty on the spectroscopic radial velocity amplitude of the sdB. If, contrary to our assumption, the *Kepler* fluxes would be severely contaminated by light from other (constant) stars, the observed beaming factor would be lower. The distribution of beaming factors from our MCMC computations is shown in Fig. 8. If the radial velocity would be measured from the Doppler beaming amplitude, using the theoretical beaming factor, the result would be 168 ± 4 km s^{-1} compared to 164.0 ± 1.9 km s^{-1} derived from spectroscopy. The uncertainty on the photometric radial velocity is dominated by the uncertainty on the theoretical beaming factor, primarily due to its dependence on the poorly known metallicity of the sdB, and to a lesser extent due to the uncertainties on the sdB's effective temperature and surface gravity.

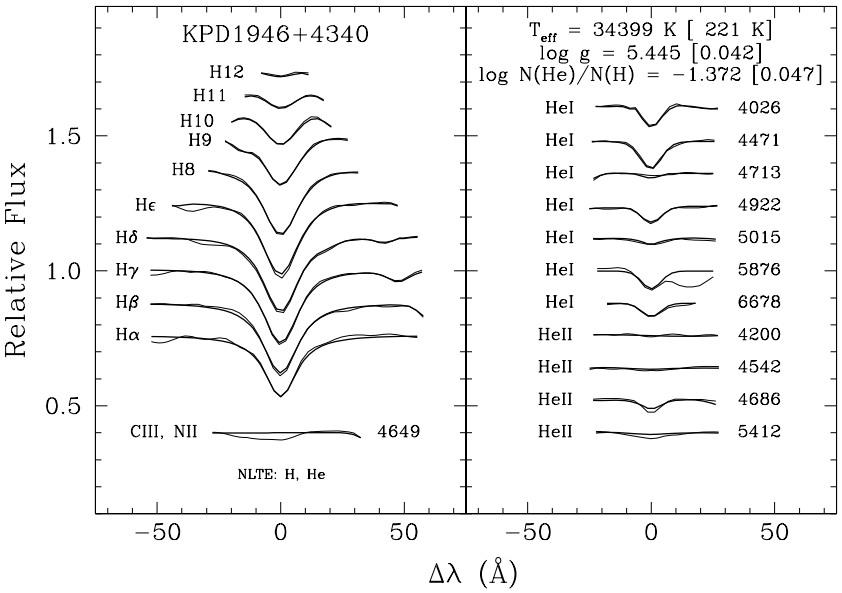

Figure 6. Fit (bold lines) to the spectral lines of KPD 1946+4340 using non-LTE sdB models, assuming zero metals.

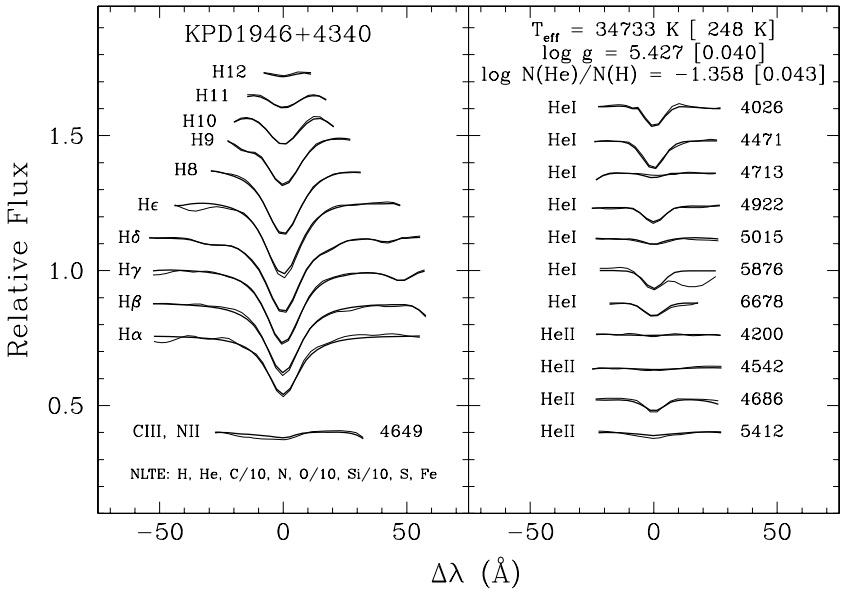

Figure 7. Fit (bold lines) to the spectral lines of KPD 1946+4340 using non-LTE sdB models, assuming a Blanchette metal composition.

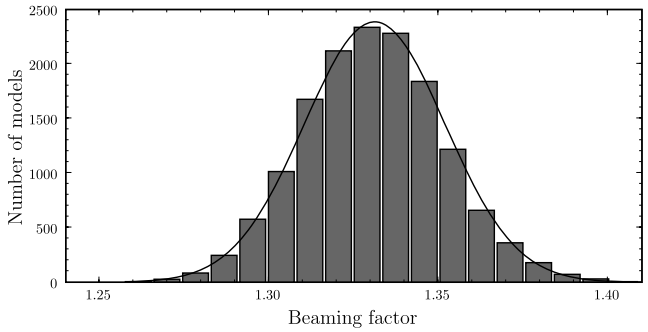

Figure 8. Distribution of the sdB's beaming factor for an MCMC run (using the mass–radius constraint for the WD; see text for details). The beaming factor is found to be $\langle B \rangle = 1.33 \pm 0.02$, which is in agreement with the theoretically expected $\langle B \rangle = 1.30 \pm 0.03$.

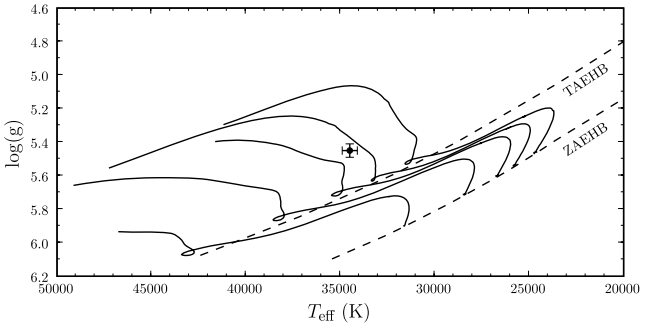

Figure 9. The sdB of KPD 1946+4340 in the $T_{\rm eff}$–log g plane. The theoretical ZAEHB and TAEHB for a 0.47 $M_\odot$ sdB are shown, together with evolutionary tracks for different envelope thicknesses (10^{-4}, 10^{-3}, 2×10^{-3}, 3×10^{-3} and 4×10^{-3} $M_\odot$). The sdB is found to be in the post-EHB phase.

Under the assumption of corotation, we find a projected rotational velocity of the sdB of $v \sin(i) = 26.6 \pm 0.8\,{\rm km\,s^{-1}}$. From spectroscopy and using LTE models with 10 times solar metallicity, Geier et al. (2010) found $v \sin(i) = 26.0 \pm 1.0\,{\rm km\,s^{-1}}$, which is in agreement with our photometric result. We conclude that the assumption of corotation is likely to be correct.

The spectroscopically determined surface gravity of the sdB ($\log g = 5.43 \pm 0.04$ and 5.45 ± 0.04 using atmosphere models with and without metals, respectively) agrees perfectly with the surface gravity of 5.452 ± 0.006 we derived from the mass–radius distribution of our light-curve models.

As concluded earlier by Morales-Rueda et al. (2003), the sdB is probably in a post-EHB phase. This is illustrated in Fig. 9, which shows the zero-age extended horizontal branch (ZAEHB) and the terminal-age extended horizontal branch (TAEHB) for an sdB with a typical core mass of 0.47 $M_\odot$, together with evolutionary tracks for different hydrogen envelope masses (10^{-4}, 10^{-3}, 2×10^{-3}, 3×10^{-3} and 4×10^{-3} $M_\odot$) from Kawaler & Hostler (2005).

Because of its low surface gravity, the sdB component of KPD 1946+4340 falls in a region of the $T_{\rm eff}$–log g plane relatively far from the centre of the instability strip. However, at least one pulsator exists in this region of the $T_{\rm eff}$–log g plane, V338 Ser, that should be in a post-EHB phase (see Østensen 2009, fig. 3). Moreover,'transient pulsators' with varying pulsation amplitudes that can go down to undetectable values in a particular epoch might exist (see the case of KIC 2991276 in Østensen et al. 2010a). For these reasons, and because we found at least one candidate p-mode pulsation frequency, it is worth continuing a photometric monitoring by *Kepler*.

The WD mass implies that it is a CO WD. The progenitor of the sdB must have been the less massive star in the original binary and by the time it reached the ZAEHB, the WD was already cooling. The accretion of material by the WD does not change the WD's internal energy content significantly (see e.g. related work on cataclysmic variables by Townsley & Bildsten 2002). The cooling time of the WD therefore sets an upper limit to the time since the sdB was on the ZAEHB. For our best estimates of the temperature and mass of the WD, the cooling tracks of Holberg & Bergeron (2006) indicate that it has been cooling for about 155–170 Myr (depending on the unknown envelope composition). The sdB's evolution from the ZAEHB to its current post-EHB-phase took 125–145 Myr (Kawaler & Hostler 2005, depending on the exact current evolutionary stage),

which means that the sdB must have formed very shortly after the WD.

6 SUMMARY

We have analysed a 33.5-d short cadence *Kepler* light curve of KPD 1946+4340, as well as low-resolution spectroscopy. In the light curve, primary and seconday eclipses, ellipsoidal modulation and Doppler beaming are detected. We model the binary light curve, taking into account the Doppler beaming and gravitational lensing effects. System parameters and uncertainties are determined using MCMC simulations.

The binary is found to consist of a $0.59 \pm 0.02\,M_{\odot}$ WD and a $0.47 \pm 0.03\,M_{\odot}$ post-EHB sdB star. The surface gravity and corotation rotational velocity of the sdB as derived from the light-curve models are found to be consistent with spectroscopic values. The observed Doppler beaming amplitude is in perfect agreement with the amplitude expected from spectroscopic radial velocity measurements. It would thus have been possible to derive the radial velocity amplitude of the sdB from the *Kepler* light curve directly.

Subtracting a good light-curve model allowed us to search for stellar oscillations. No significant stellar variability of the sdB or WD could be detected yet. At least one candidate p-mode pulsation frequency was found, however, and the sdB can also possibly be a transient pulsator. KPD 1946+4340 continues to be observed by *Kepler*.

ACKNOWLEDGMENTS

We thank the referee Martin van Kerkwijk for his helpful suggestions. The authors gratefully acknowledge everybody, who has contributed to make the *Kepler Mission* possible. Funding for the *Kepler Mission* is provided by NASA's Science Mission Directorate. Part of the data presented here have been taken using ALFOSC, which is owned by the Instituto de Astrofísica de Andalucia (IAA) and operated at the Nordic Optical Telescope (Observatorio del Roque de los Muchachos, La Palma) under agreement between IAA and the NBIfAFG of the Astronomical Observatory of Copenhagen. This research also made use of data taken with the Bok telescope (Steward Observatory, Kitt Peak). The research leading to these results has received funding from the European Research Council under the European Community's Seventh Framework Programme (FP7/2007–2013)/ERC grant agreement no. 227224 (PROSPERITY), as well as from the Research Council of K.U.Leuven grant agreement GOA/2008/04. During this research, TRM was supported under grants from the UK's Science and Technology Facilities Council (STFC, ST/F002599/1 and PP/D005914/1).

REFERENCES

Agol E., 2002, ApJ, 579, 430
Agol E., 2003, ApJ, 594, 449
Allard F., Wesemael F., Fontaine G., Bergeron P., Lamontagne R., 1994, AJ, 107, 1565
Blanchette J., Chayer P., Wesemael F., Fontaine G., Fontaine M., Dupuis J., Kruk J. W., Green E. M., 2008, ApJ, 678, 1329
Cardelli J. A., Clayton G. C., Mathis J. S., 1989, ApJ, 345, 245
Claret A., 2004, A&A, 428, 1001
Collier Cameron A. et al., 2007, MNRAS, 380, 1230
Copperwheat C. M., Marsh T. R., Dhillon V. S., Littlefair S. P., Hickman R., Gänsicke B. T., Southworth J., 2010, MNRAS, 402, 1824
de Kool M., 1990, ApJ, 358, 189
Degroote P. et al., 2009, A&A, 506, 471
Downes R. A., 1986, ApJS, 61, 569
Gänsicke B. T., Beuermann K., de Martino D., 1995, A&A, 303, 127
Geier S., Heber U., Podsiadlowski P., Edelmann H., Napiwotzki R., Kupfer T., Mueller S., 2010, A&A, 519, A25
Gilliland R. L. et al., 2010a, PASP, 122, 131
Gilliland R. L. et al., 2010b, ApJ, 713, L160
Gould A., 1995, ApJ, 446, 541
Green E. M., Fontaine G., Hyde E. A., For B., Chayer P., 2008, in Heber U., Jeffery C. S., Napiwotzki R., eds, ASP Conf. Ser. Vol. 392, Hot Subdwarf Stars and Related Objects. Astron. Soc. Pac., San Francisco, p. 75
Haas M. R. et al., 2010, ApJ, 713, L115
Han Z., Podsiadlowski P., Maxted P. F. L., Marsh T. R., Ivanova N., 2002, MNRAS, 336, 449
Han Z., Podsiadlowski P., Maxted P. F. L., Marsh T. R., 2003, MNRAS, 341, 669
Heber U., 1986, A&A, 155, 33
Heber U., 2009, ARA&A, 47, 211
Heber U., Reid I. N., Werner K., 2000, A&A, 363, 198
Hills J. G., Dale T. M., 1974, A&A, 30, 135
Holberg J. B., Bergeron P., 2006, AJ, 132, 1221
Hu H., Nelemans G., Østensen R., Aerts C., Vučković M., Groot P. J., 2007, A&A, 473, 569
Jenkins J. M. et al., 2010, ApJ, 713, L120
Kawaler S. D., Hostler S. R., 2005, ApJ, 621, 432
Koch D. G. et al., 2010, ApJ, 713, L79
Lemke M., 1997, A&AS, 122, 285
Loeb A., Gaudi B. S., 2003, ApJ, 588, L117
Maeder A., 1973, A&A, 26, 215
Marsh T. R., 2001, MNRAS, 324, 547
Maxted P. F. L., Marsh T. R., North R. C., 2000, MNRAS, 317, L41
Morales-Rueda L., Maxted P. F. L., Marsh T. R., North R. C., Heber U., 2003, MNRAS, 338, 752
Østensen R. H., 2009, Commun. Asteroseismol., 159, 75
Østensen R. et al., 2010a, MNRAS, in press
Østensen R. H. et al., 2010b, A&A, 513, A6
Saffer R. A., Bergeron P., Koester D., Liebert J., 1994, ApJ, 432, 351
Sahu K. C., Gilliland R. L., 2003, ApJ, 584, 1042
Shakura N. I., Postnov K. A., 1987, A&A, 183, L21
Townsley D. M., Bildsten L., 2002, ApJ, 565, L35
Van Grootel V. et al., 2010, ApJ, 718, L97
van Kerkwijk M. H., Rappaport S. A., Breton R. P., Justham S., Podsiadlowski P., Han Z., 2010, ApJ, 715, 51
Verbunt F., Rappaport S., 1988, ApJ, 332, 193
von Zeipel H., 1924, MNRAS, 84, 665
Wesemael F., Fontaine G., Bergeron P., Lamontagne R., Green R. F., 1992, AJ, 104, 203
Zucker S., Mazeh T., Alexander T., 2007, ApJ, 670, 1326

This paper has been typeset from a TEX/LATEX file prepared by the author.